Sustainable Chemistry and Pharmacy 27 (2022) 100678

Contents lists available at ScienceDirect

Sustainable Chemistry and Pharmacy

journal homepage: www.elsevier.com/locate/scp

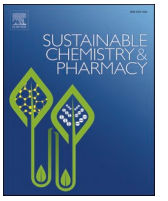

The challenge to produce magnetic nanoparticles from waste containing heavy metals aiming at biomedical application: New horizons of chemical recycling

Mauro Flores Polenz [b], Luis Guilherme Giannina Sante [a], Eduardo Malschitzky [b], Alesandro Bail [a,*]

[a] Grupo de Química de Materiais de Tecnologias Sustentáveis (GQMATS), Universidade Tecnológica Federal do Paraná (UTFPR), CEP: 86812-460, Londrina (PR), Brazil

[b] Programa de Pós Graduação em Medicina Animal - EQUINOS (PPGMA-Equinos, Universidade Federal do Rio Grande do Sul (UFRGS), CEP: 91540-000, Porto Alegre (RS), Brazil

ARTICLE INFO

Keywords:
Silica-coated magnetite
Green synthesis
Biocompatibility
Spermatozoon immobilization

ABSTRACT

Silica-coated magnetite nanoparticles (SMNPs) were prepared by a green approach based on waste pickling acid. A set of techniques (PXRD, ATR, VSM, SEM, TEM, DLS and XPS) was used for their characterization, and for monitoring the levels of heavy metal impurities. The SMNPs presented an expected profile, similar to that reported for nanoparticles produced from fresh chemicals. The crystallinity and magnetic saturation confirmed the formation of the Fe_3O_4 phase, silanol and siloxane absorption bands, as well as TEM images confirmed the coating SiO_2. The SMNPs chosen for the biomedical tests did not present a significant level of contaminants, and the non-toxic silica coat produced by the sol-gel method ensured a preliminary study on its biocompatibility with reproductive cells in vitro. SMNPs presented a high ability to immobilize spermatozoon cells, suggesting that a fine control of their surface charge must be carried out for specific biomedical purposes. The agglomeration of the solid NPs was evidenced by SEM and by DLS measurements. Its aggregation was tuned by sonication, and a 5-min long ultrasound treatment was capable of halving the agglomerate size, allowing a one-to-one interaction (one SMNPs agglomerate to each cell). The CASA system used to monitor the semen quality showed that vigor, motility and velocity parameters were kept at levels very close to the control group. Finally, a waste-based input submitted to a meticulous purification process could be used as a source for magnetic materials synthesis and evaluated in the biomedical field as long as all precautions are taken into account.

1. Introduction

The reuse of industrial waste as an alternative to save mineral resources has gained relevance due to the demands for more sustainable processes as those predicted by circular economy standards (Matlin et al., 2020). Certainly, it has to be considered that proposals involving application in the biomedical field raise discussions regarding aspects of toxicity and pre-established limits for hazardous compounds, which is totally plausible since, besides health and welfare, ethical issues are at stake (Joseph et al., 2021; Višak

* Corresponding author.
E-mail address: alebail@utfpr.edu.br (A. Bail).

https://doi.org/10.1016/j.scp.2022.100678
Received 31 December 2021; Received in revised form 3 March 2022; Accepted 21 March 2022
Available online 6 April 2022

and Garner, 2016). The fact is that several initiatives have changed the concept of waste, such as the use of recycled wastewater as clean water or in sanitary applications (Tortajada, 2020; Tortajada and van Rensburg, 2019), and the use of food waste for livestock feeding (Dou et al., 2018). These initiatives and many others are supported by the Green Chemistry's principles (Friege, 2017), as well as by the 17 Life-Changing Goals established by the United Nations in 2015 (UN, 2022).

In that context, the waste pickling acid (WPA), which is an iron-rich effluent produced worldwide as a result of the steel surface pre-treatment in galvanizing plants, appears as a potential source of iron ions for dozens of industrial processes despite the high load of contaminants. It is estimated that around 300,000 tons of WPA have been generated annually only in the European Union, and in turn, the conventional treatments, which usually involve precipitation with limestone, have been responsible for large amounts of metals-containing sludge formation (Zueva et al., 2021). In addition, several alternatives have been proposed to overcome this issue and such strategies are capable of recovering both acid and metal in order to produce iron-based inputs, such as iron salts and magnetic oxides (Tang et al., 2016; Tsai et al., 2021; Wang and Lv, 2018). Despite that, some of them run into difficulties related to high energy costs (Özdemir et al., 2006), and there seems not to be a consistent report evaluating the biocompatibility of these recycled inputs in the biomedical field.

One of the biggest challenges in using residual sources for the preparation of materials for the biomedical field is the presence of a high content of hazardous ionic species, such as chromium, zinc and lead. Some of these chemicals have a well-known carcinogenic effect and cannot come into contact with living cells because they can ultimately lead them to death (Eastmond et al., 2008). Therefore, the use of magnetic oxides from WPA for biomedical purposes must take into account strategies to block the contact between the magnetic surface and the biological medium, for instance by forming a protective silica layer as find in core-shell structures (Zelepukin et al., 2017).

Silica-coated magnetite nanoparticles (SMNPs), i.e. core-shell structures, which are part of nanotechnology strategies, have been extensively investigated and proposed as a kind of flagship for innovative technologies in the biomedical area, mainly due to three advantages: (i) the ferrimagnetism of its core, (ii) the reactive and tunable SiO_2 surface amenable to chemical modifications, and (iii) its biocompatibility (Rodriguez et al., 2017; Sonmez et al., 2015). In addition to more traditional studies, such as those in which SMNPs are investigated as adsorbents for wastewater treatment (Kumari et al., 2019) or photocatalyst for degradation of organic dyes (Kumar et al., 2016), these nanomaterials have been studied in fields such as hyperthermia, drug release, tissue engineering, therapeutic diagnosis, and lab-on-a-chip approach, due to their exclusive chemical and physical properties (Cardoso et al., 2017).

In this type of application, there is a clear demand for discrete nanoparticles, small enough to cross the plasma membrane and access the inner of the cells (Foroozandeh and Aziz, 2018). In an outer surface approach, however, there is a concern with the non-violation of the cell membrane, as well as with the maintenance of its inner information. Therefore, as the average size for equine spermatozoa head includes 5.3–6.6 μm of length and 2.8–3.3 μm of a maximum width (Larentis et al., 2018), sub or micrometric magnetic particles formed by agglomeration of magnetite nanoparticles can prevent the aforementioned possible damages to the cells and offer an anatomical platform to the interaction with them.

Biocompatibility of these (nano)materials have been evaluated mainly in vitro, and the few examples of in vivo approaches have been restricted to small organisms (Shabana et al., 2021; Samrot et al., 2021). In general, results have pointed out that SMNPs are less toxic and more biocompatible than other metal NPs, appearing as an ideal metallic NP for biomedical application (Guo et al., 2018). Moreover, the use of novel strategies to support genetic improvement has been extensively investigated as a way to develop more sustainable techniques for energy and water saving, including several advantages for animal breeding and other activities belonging to the livestock sector (Monteiro et al., 2021; Thornton, 2010). Although there are many studies reinforcing the biocompatibility of these materials (Sun et al., 2006; Sonmez et al., 2015; Tran et al., 2022) and other showing the feasibility of synthesizing magnetic nanoparticles from WPA (Zhang et al., 2015; Cunha et al., 2021), approaches involving residual sources are scarce.

In this work we propose a green strategy in which an industrial waste, previously treated to remove hazardous chemical species and prevent large contamination by heavy metals, was used to synthesize magnetic nanoparticles coated by a non-toxic mesoporous silica layer and submit them to the direct contact with reproductive equine cells in order to perform an assessment of its in vitro biocompatibility.

2. Materials and methods

2.1. Materials

The waste pickling acid (WPA) used as a source for iron(II) ions for the waste-based SMNPs was gently provided by a local company and had its chemical composition previously analyzed by us (Cunha et al., 2021). Tetraethylortosilicate (TEOS) was purchased from Sigma-Aldrich, whereas iron(II) chloride tetrahydrate ($FeCl_2 \bullet 4H_2O$) and iron(III) chloride hexahydrate ($FeCl_3 \bullet 6H_2O$) were purchased from Reagen. Hydrochloric acid, ammonia aqueous solution and absolute ethanol, all reagent grade, were purchased from Neon. The commercial diluent Equipure® was purchased from Minitube (Germany). Unless otherwise specified, reagents were used as received without further purification.

2.2. Synthesis of the SMNPs

Silica-coated magnetite nanoparticles (SMNPs) were prepared by the co-precipitation method followed by the sol-gel process according to the literature (Pasandideh et al., 2016). Fresh iron salts were used in the preparation of the control magnetite, whereas $FeCl_2 \bullet 4H_2O$ from WPA was used in the other syntheses. In order to obtain the compound $FeCl_2 \bullet 4H_2O$, the WPA was treated as reported previously by us (Cunha et al., 2021). The syntheses were carried out as follows: 5.0 mmol of $FeCl_3 \bullet 6H_2O$ and 2.5 mmol of $FeCl_2 \bullet 4H_2O$ were separately dissolved in 5.0 mL of a 0.5 M HCl aqueous solution and 3.0 mL of distilled water, respectively. Upon the dissolution,

both solutions were transferred to a 3-necked glass flask containing 80 mL of distilled water. After sealing the flask with rubber septa, a nitrogen purging was performed in order to eliminate the oxygen from air inside the flask and then the reaction system was heated up to 80 °C under vigorous magnetic stirring. After that, 10 mL of concentrated NH_3 aqueous solution was dropwise added using a polypropylene syringe to achieve pH 12–13 and the formation of a black slurry (magnetite) which was kept under magnetic stirring for 30 min. The uncoated magnetite prepared from fresh chemicals was reserved for comparative purposes.

Upon waste-based magnetite synthesis, the surface coating with silica was carried out by the dropwise addition of 0.6 mL (2.69 mmol) of TEOS over the reaction mixture at the same experimental conditions applied in the previous step. Then, the reaction mixture was sonicated for 30 min and left to rest for 24 h at room temperature. Finally, the magnetic material was decanted by using a neodymium magnet and exhaustively washed with distilled water, until the supernatant presented a pH 7–8, which was followed by a last wash with 50 mL of absolute ethanol. The SMNPs obtained were dried at room temperature for 24 h and then stored in propylene flasks. Additionally, two more coating reactions were performed using 2.5 mL (11.2 mmol) and 5.6 mL (25.1 mmol) of TEOS in order to evaluate its influence on the coating thickness. Therefore, the samples were labeled as follows: control magnetite (prepared from fresh chemicals), SMNP-1 (0.6 mL of TEOS), SMNP-2 (2.5 mL of TEOS) and SMNP-3 (5.6 mL of TEOS), all prepared using iron(II) chloride tetrahydrate obtained from WPA.

2.3. Techniques for characterization of the SMNPs

Powder X-ray diffraction analysis (PXRD) was conducted in a Bruker diffractometer model D2 Phaser operating at 30 kV and 10 mA with copper radiation (Cu-K_α = 0.15418 nm), with graphite monochromator in the range of 10–60° with dwell time of 2°/min. The average crystallite size was estimated using the Debye-Scherrer equation ($D = K\lambda/\beta\cos\theta$), where D is the average crystallite size, K = 0.9082 is the Scherrer constant for cubic crystallites (Langford and Wilson, 1978), λ is the wavelength of the X-ray beam, β is the corrected peak width (full width at half maximum, FWHM) obtained by fitting a Gaussian function, and θ is the Bragg diffraction angle of the strongest peak (Shahid et al., 2019).

Scanning electron microscopy (SEM) was recorded in an FE-SEM (TESCAN, model MIRA 3 LMU, Brno, Kohoutovice, Czech Republic). Around 10 mg of the sample was dispersed in 1 mL of water and one drop of the suspension was placed in the sample holder in order to evaporate the solvent at 30 °C for 10 min.

Transmission electron microscopy (TEM) was performed in a JEOL JEM 1200EX-II with resolution up to 0.5 nm. Images were registered using a high-resolution camera CCD Gatan (Orius SC1000B). Samples were placed in grids, metalized with gold and dried in an oven before analysis.

The infrared spectra were registered in a Thermo Scientific spectrophotometer, model Nicolet iS5 iD5, using the attenuated total reflectance (ATR) mode. A sample was placed over an equipment window and the measurements were performed with 16 scans and 4 cm^{-1} of resolution.

Vibrating-sample magnetometry analysis (VSM) was performed in a magnetometer (VSM MicroSense, Model 32 KP Gaussmeter) to evaluate the magnetic properties of magnetic nanoparticles at 303 K with a swept magnetic field between −15 and 15 kOe.

X-ray photoelectron spectroscopy analysis (XPS) was carried out with SPECS equipment working with X-ray monochromatic radiation from an Al anode and a hemispherical energy analyzer PHOIBOS 150. Charge accumulation was reduced with a food gun (FG500).

Particle size in aqueous solutions was measured by dynamic light scattering (DLS) using an Anton Paar equipment, model Litesizer 500. Around 10 mg of the powder sample was dispersed in 10 mL of distilled water, shaken by hand and immediately measured thereafter.

The interaction between cells and SMNPs was analyzed in an optical microscope (magnification of 1,000X) coupled to a digital camera.

2.4. Biocompatibility evaluation

The interaction between SMNPs and animal cells was evaluated using equine semen obtained from a Brazilian specialized breeding center. Four stallions had their sperm collected considering three ejaculations each. The spermatozoon had its concentration set to 50 × 10^6 mL^{-1} using a commercial diluent (EquiPure®, Minitube Germany®) and immediately separated into groups. The groups that received treatment were incubated for 5 min at room temperature and mixed to 8.0 or 16.0 mg of SMNPs for each 500 × 10^6 spermatozoa. After that, a neodymium magnet was approached for 15 min to promote the separation of SMNPs from the liquid medium. Upon this step, the cells were evaluated in comparison to the control test. All analyses were carried out using the CASA system for spermatic analysis (MACE sperm tracker®, Antúrius Brasil®) with the same setup. The standards used for the equipment setup were based on the recommendations of the program MACE sperm tracker® for the analysis of the semen from equines considering the following parameters: captured nanoparticles size ranging from 1 to 61 $pixels^2$, spermatozoon considered immobile (<5 μms^{-1}), slow (<40 μms^{-1}), intermediate (from 45 to 90 μms^{-1}), or fast (above 90 μms^{-1}); progressives with straightness >70%, circular with linearity <45%, and acquisition rate of 17 images per second. At least three fields randomly chosen and 500 spermatozoa were evaluated for each sample according to the following parameters: concentration (10^6 spermatozoon mL^{-1}), total motility (TM, %), progressive motility (PM, %), vigor (1–5), as well as curvilinear velocity (VCL, μms^{-1}), linear velocity (VSL, μms^{-1}), and average path velocity (VAP, μms^{-1}).

3. Results and discussion

3.1. Characterization of the SMNPs

Considering the need for strictly controlled conditions regarding biomedical application and a possible chemical contamination by materials produced from a secondary source, the first challenge was to ensure the absence of hazardous chemical species in the precursor iron(II) chloride tetrahydrate. For this reason, the WPA was carefully treated and characterized as reported earlier by us (Cunha et al., 2021). According to the previous results, the heavy metals concentration in the iron(II) chloride tetrahydrate crystals was relatively low, with lead, chromium and nickel totaling no more than 50 mg kg^{-1}, whereas zinc achieved up to 2.23 wt%.

SMNPs produced from pre-cleaned secondary sources were characterized by a set of techniques before testing of biological material in order to prevent any deleterious effects arising from possible contamination by heavy metals.

3.2. Characterization of the SMNPs

The PXRD patterns of the synthesized materials are shown in Fig. 1. The uncoated magnetite (Fig. 1a) presented a typical set of diffraction peaks positioned at 30.2, 35.6, 43.3, 53.8 and 57.3° (2θ), referring to the diffraction planes (220), (311), (400), (422) and (511), respectively. This set of peaks is in agreement with JCPDS card no. 85–1436, confirming the synthesis of magnetite in its close-packed cubic arrangement by the co-precipitation method (Silva et al., 2013). The silica-coated materials (Fig. 1 b-d) had a profile similar to that of the magnetite. Indeed, all the diffraction peaks showed the same position and relative intensity compared to the control material. The different amounts of TEOS, used to modulate the thickness of the silica coating, did not cause significant interference, except for the discrete halo-amorphous between 20 and 30° (2θ) for both materials in which a higher amount of TEOS was added. Such halo-amorphous, as is widely known, is typical of amorphous silica and represents the disordered SiO_4 unit arrangement of the porous silica coating formed on the magnetite (Sharma et al., 2016). The relatively wide peaks indicate the presence of nanostructured materials, which was confirmed by Debye-Scherrer's calculations for the synthesized materials based on the (311) diffraction plane. The size of the magnetite crystallites was 97.2, whereas for SMNP-1, SMNP-2 and SMNP-3 the sizes of the crystallites were 129.4, 119.7 and 94.2, respectively (Fig. 1). The results show that the amount of TEOS employed in the coating step has influenced the crystallites growth, making them smaller the more TEOS was added. Several factors can cause this effect, but literature reports the Zener pinning, which is caused by the presence of a small amount of a second phase in the system, as an important suppressor of size in grain boundary diffusion processes (Hu et al., 2021). A second solid phase based on mesoporous silica nanoparticles may have been favored by the increase in the TEOS amount used in the coating step. In fact, the Fe(II)/TEOS molar ratio used in the syntheses was 0.5 for SMNPs-1 and 5.0 for SMNPs-3, which may represent a large excess of SiO_2 and may explain the observed effect.

The infrared spectra are shown in Fig. 2. This is a useful technique for preliminary characterization of silica-coated nanoparticles because of the existence of typical vibrational modes of silica chemical bonds in the region ranging from 750 to 1120 cm^{-1}. Therefore, the coating process could be confirmed based on the variation of the TEOS volume. Fig. 2a shows that magnetite presented a wide absorption band centered at 600 cm^{-1} referring to iron-oxygen stretching modes (νFe-O), whereas the silica-coated nanoparticles presented two wide absorption bands at 794 and 1094 cm^{-1}, referring to siloxane stretching modes (νSi-O-Si), as well as another absorption band centered at 957 cm^{-1} referring to the silanol stretching mode (νSi-OH) (Fig. 2b–d). The coated nanoparticles kept the νFe-O vibrational mode of medium-strong intensity independently of the amount of silica deposited on the magnetite, suggesting that

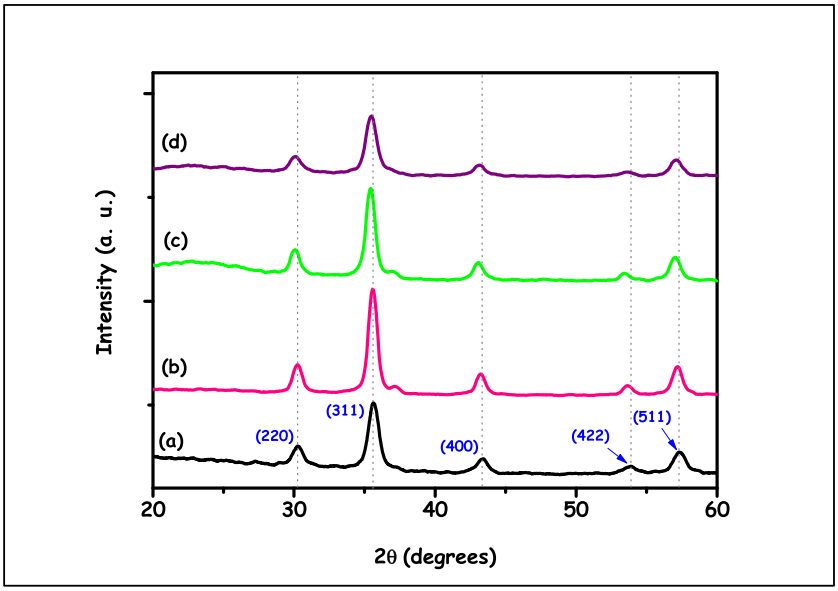

Fig. 1. PXRD patterns for (a) control magnetite, prepared from fresh inputs, (b) SMNP-1, (c) SMNP-2 and (d) SMNP-3, prepared using iron(II) chloride tetrahydrate from WPA.

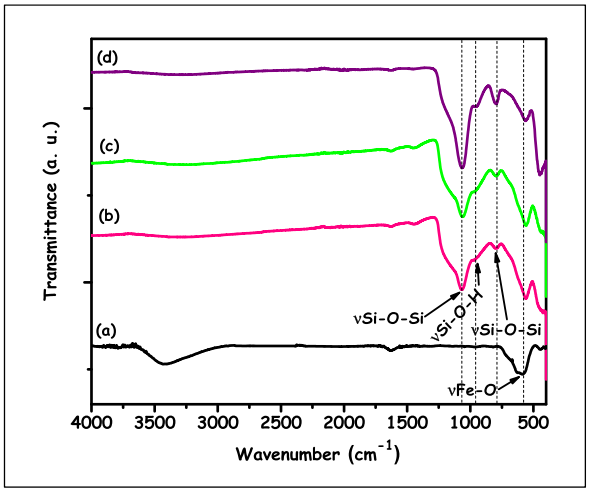

Fig. 2. Infrared spectra for (a) control magnetite, (b) SMNP-1, (c) SMNP-1, and (d) SMNP-3 highlighting absorption bands referring the silica shell and magnetite core.

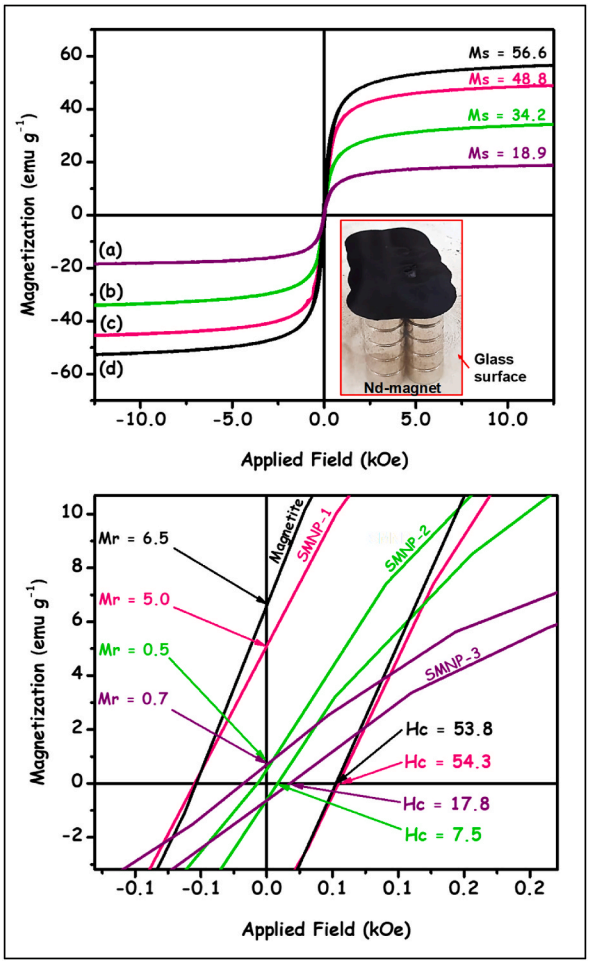

Fig. 3. VSM analysis for control magnetite and SMNPs synthesized. (top) VSM curves and (inset) an image of the NPs being attracted by the Nd magnet over a glass surface. (down) A detail of the magnetic curves highlighting the hysteresis of the materials.

the magnetic inner withstood the reaction steps. All vibrational modes shown in Fig. 2 are in agreement with the literature, and specifically the Si–O modes confirm a successful coating process (Safari et al., 2016). In addition, control magnetite presented a broad band centered at 3400 cm^{-1} referring to OH stretching from adsorbed water and hydroxyl groups of the magnetite surface. This absorption band was less intense in the silica-coated materials, which could have been a result of the desiccator storage process before analysis.

VSM analysis was performed to characterize the magnetic properties of the synthesized materials prepared from secondary sources. The obtained results for the four synthesized materials can be seen in Fig. 3. Some useful parameters extracted from the hysteresis loops include saturation magnetization (Ms), remanence (Mr), and coercivity (Hc). The uncoated magnetite (control magnetite) presented a typical hysteresis loop for a ferrimagnetic material, with Ms = 56.6 emu g^{-1}, Mr = 6.5 emu g^{-1} and Hc = 53.8 Oe. These values are within the usual range reported in the literature, in which the Ms ranges from 54 to 84 emu g^{-1} as a function of the crystallite size. In

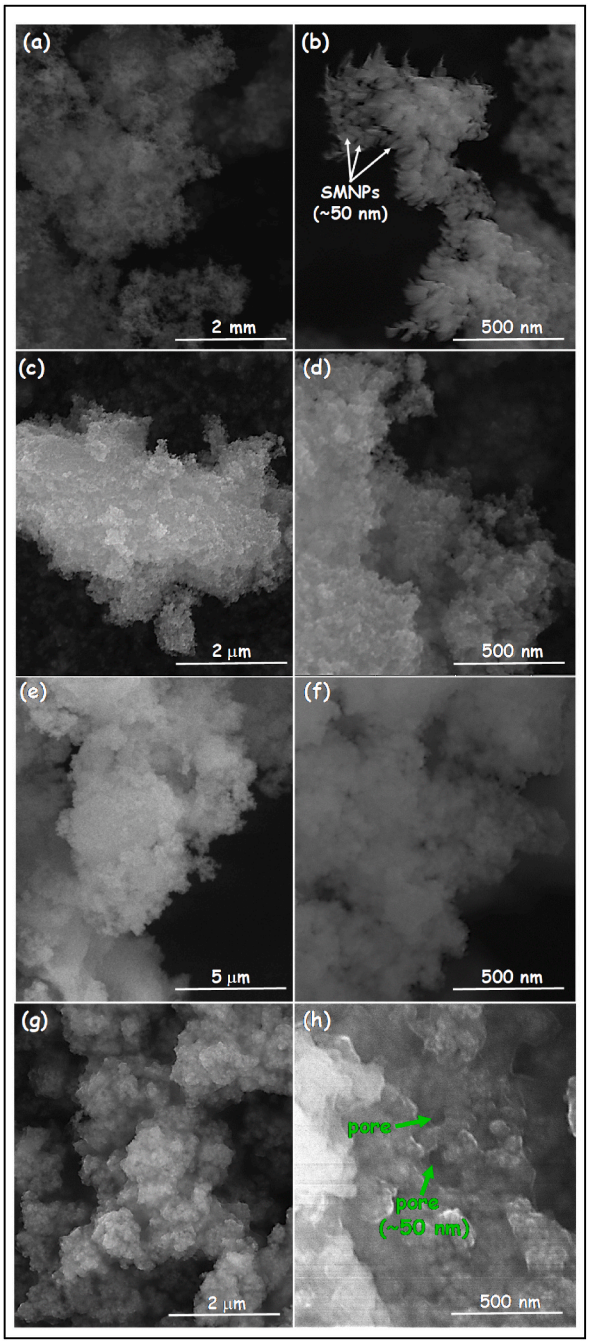

Fig. 4. SEM images of (a, b) control magnetite, (c, d) SMNP-1, (e, f) SMNP-2 and (g, h) SMNP-3.

fact, the obtained Ms (56.6 emu g^{-1}) seems to be slightly low when the average crystallite size (97.2 nm) is considered, however, other studies have presented similar results (Rahmawati et al., 2017). For comparative purposes, the Ms for bulk magnetite was theoretically estimated to be 92 emu g^{-1} (Li et al., 2017).

The silica-coated materials had different VSM results from each other. The SMNP-1, the one prepared with a thinner layer of mesoporous silica, showed magnetic results close to those obtained for the magnetite, that is, Ms = 48.8 emu g^{-1}, Mr = 5.0 emu g^{-1}, and Hc = 54.3 Oe. In its turn, SMNP-2 and SMNP-3 presented a decrease in their Ms values, suggesting an equivalent decrease in the size of their crystallites.

It is well known that the smaller the particles, the lower the saturation magnetization Ms (Novoselova, 2021), therefore, the lower values of Ms obtained for SMNP-2 and SMNP-3 suggest the existence of smaller crystallites, which is in agreement with the decrease in the average crystallite size calculated by the Debye-Scherrer's equation (Kemp et al., 2016; Kelgenbaeva et al., 2013).

The morphology of the synthesized SMNPs and control magnetite was studied by SEM analysis and the results are shown in Fig. 4. Firstly, Fig. 4a and b shows that the non-coated magnetite forms micrometric agglomerates, with nanoparticles around 50 nm in size. It is possible to notice in the images that the non-coated magnetite seems to present nanoparticles of a more homogeneous shape. Upon the coating process by silica, SMNP materials seem to have gone through a densification process, increasing their agglomeration level and making it difficult to identify discrete nanoparticles (Fig. 4c–f). Specifically for SMNP-3, a higher level of agglomeration is observed, confirming the formation of micrometric agglomerates. Additionally, SMNP-3 showed nanometric pores, with size around 50 nm (Fig. 4h).

In order to further elucidate the morphology of the nanoparticles, the SMNP-1 was submitted to TEM analysis and the images are shown in Fig. 5. The nanocrystallites of magnetite were embedded in a bounding silica shell as depicted in Fig. 5a and e, confirming the formation of a core-shell structure. The magnification of Fig. 5b shows that SMNP-1 nanoparticles have a size around 15 nm and a thin SiO_2 edge, as indicated by the orange arrow, with thickness around 3 nm, which is in agreement with the literature (Ahmad et al., 2019). However, the crystallite sizes obtained by TEM diverge from those estimated using the Debye-Scherrer equation, suggesting that the PXRD-based method presents some shortcomings when the nanoparticles undergo an intense agglomeration process. Additionally, the TEM results corroborate the existence of nanopores of approximately 50 nm, which was previously showed by SEM analysis (Fig. 5c). The size distribution of a given agglomerate of SMNP-1 nanoparticles can be seen in histogram of Fig. 5d.

In order to know both hydrodynamic size and zeta potential of the synthesized SMNPs in aqueous media, a DLS analysis was carried out and its results are shown in Fig. 6. The agglomeration of the nanoparticles in aqueous solution was confirmed by their size

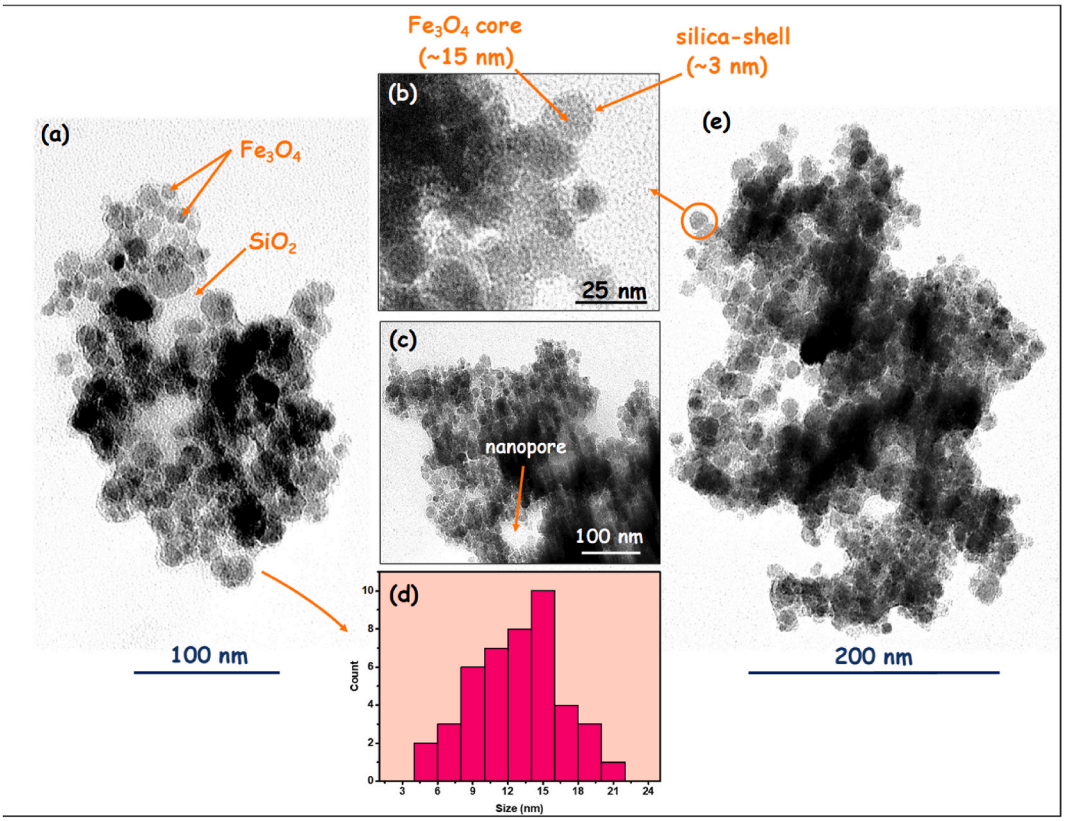

Fig. 5. TEM images of SMNP-1 showing (a) nanocrystallites of Fe_3O_4 embedded in a silica shell, (b) a detail of the core-shell structure highlighting a 15 nm wide magnetite crystallite and a silica shell of around 3 nm of thickness, (c) a nanopore around 50 nm in size, (d) size distribution on NPs, and (e) an aggregate of nanocrystallites around 200 nm wide.

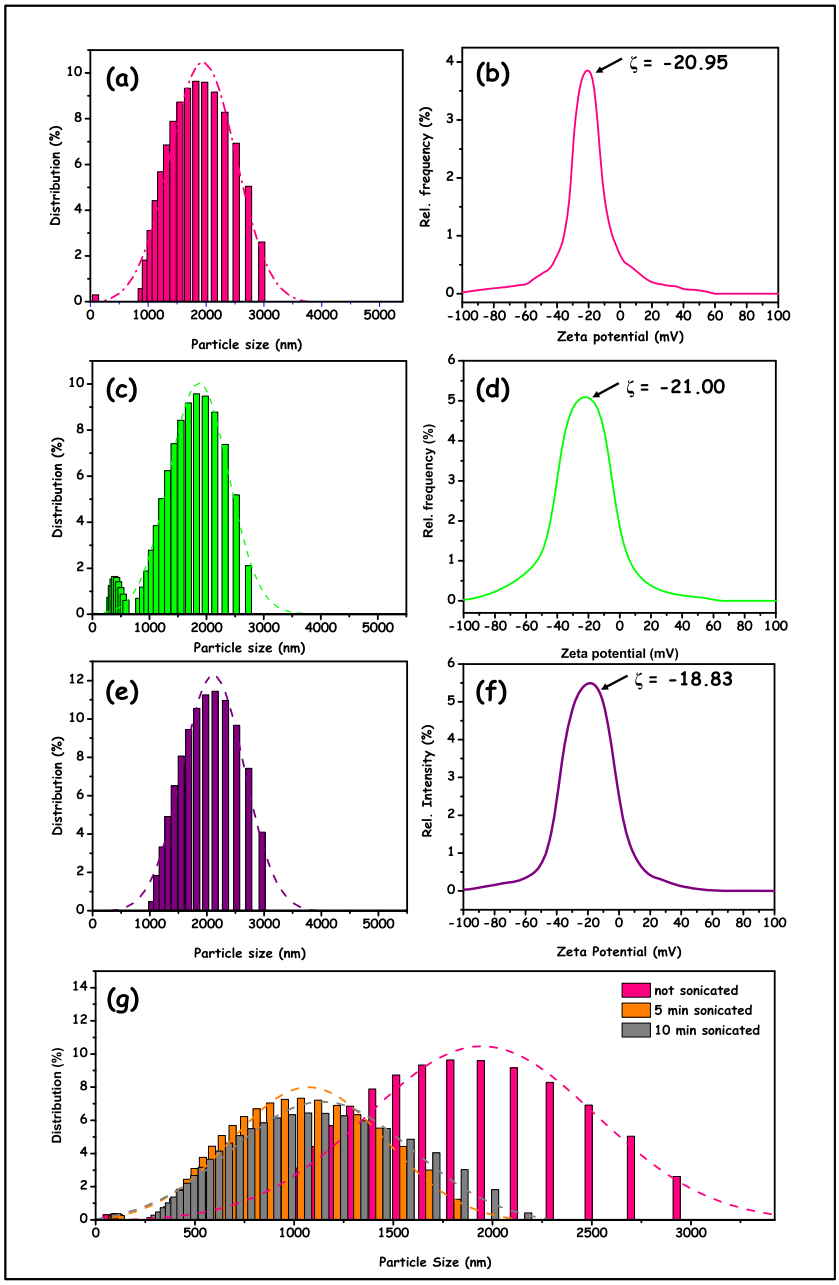

Fig. 6. Particle size distribution in aqueous solution for (a) SMNP-1, (c) SMNP-2 and (e) SMNP-3. Zeta potential for (b) SMNP-1, (d) SMNP-2, and (f) SMNP-3. (g) Effect of the ultrasonic treatment in the particle size of SMNP-1.

distribution centered at 2.0 μm (Fig. 6a, c and 6e). Aiming at investigating the possibility of reducing the size of the aggregates, the SMNP-1 was submitted to ultrasonic treatments for distinct periods of 5 and 10 min. Fig. 6f shows that the 5 min-long treatment was capable of decreasing the average size of the SMNP-1 from ~2.0 to ~1.0 μm, but no significant additional size change was observed after 10 min. These results confirm the agglomeration of the SMNPs in aqueous solution and the influence of the ultrasound on their partial deconstruction.

In terms of zeta potential, the SMNP-1 and SMNP-2 showed similarities with $\zeta = -20.95$ and $\zeta = -21.00$ mV (Fig. 6b and d), respectively, whereas SMNP-3 presented $\zeta = -18.83$ mV (Fig. 6f). These results are in agreement with the literature for silica-coated magnetite nanoparticles (Mandel et al., 2015). The difference of just over 2 mV between SMNP-3 and the others was attributed to a higher acidity of the silanol groups (Si–OH) which covers the silica surface, perhaps influenced by its higher thickness and less proximity to the magnetite core. Indeed, literature reports that in multiple-valence environments formed by different interconnected metal-oxygen units, as in the case of the interface between SiO_4 and FeO_6 units, the Tanabe's postulates predict that the –OH BrÖnsted

surface sites attached to silicon atoms can display changes in their acidity, showing a higher capacity of donating a H atom to a H_2O molecule (Tanabe et al., 1974), which may lead to a different distribution of surface charge.

As aforementioned, for this work the main challenge was the safe use of waste-based materials for biomedical applications. For this reason, SMNP-1 was chosen for further evaluation and confirmation of the absence of unwanted chemical species. Fig. 7 shows the result obtained for magnetite and SMNP-1, both submitted to XPS analysis. Considering that the synthesis of the materials was performed under conditions of high pH, the metallic ion zinc - one among the contaminants in the precursor iron(II) chloride tetrahydrate - was successfully eliminated by the formation of the tetrahydroxozincate(II) complex ion, $[Zn(OH_4]^{2-}$, highly soluble at basic conditions. In fact, no signal was detected in the range of 1020–1050 eV, typically attributed to bivalent zinc species (Chang et al., 2019). In addition, the minor contaminants and their typical ranges, that is, lead (135–145 eV), chromium (570–580), and nickel (850–885 eV), were not detected either (Bhat et al., 2016; Jin et al., 2019; Fu et al., 2018). In addition, the peaks of silicon at 104 eV (Si2s) and 154 eV (Si2p) corroborated the coating of magnetic NPs. Oxygen (O1s) peak centered at 533 eV showed a profile with almost 8 eV width, probably due to the existence of different binding energies, such as lattice oxygen (Fe–O, 530 eV), surface hydroxyl (-OH, 532 eV) and adsorbed water (-OH_2, 534 eV) (Wang et al., 2016). Still for the oxygen, another signal is present as a broader peak at 977 eV, which could be attributed to oxygen KLL due to an auger transition (Jacomaci et al., 2019; Baltrusaitis et al., 2007). Additionally, iron was detected as a weak signal at 90 eV (Fe3s) and 56 eV (Fe3p). An extra signal centered at 284 eV was attributed to the interference from the carbon-based tape used to stick the powder samples to the sample holder. Fig. 7a and b shows the expected signals for the components of the materials, such as $Fe2p_{1/2}$ and $Fe2p_{3/2}$ at 725 and 710 eV, respectively, confirming the preferential synthesis of Fe_3O_4 and an almost negligible presence of satellite peak at 719 eV and 723 eV, which are characteristics of γ-Fe_2O_3 and FeOOH (Tian et al., 2011). Nevertheless, any material synthesized in this work could show some degree of oxidation due to the drying process performed at room atmosphere.

3.3. Biocompatibility tests

Among all analyzed parameters, only progressive motility presented a significant difference ($P < 0.05$) between the control group (CG) and the test groups (T1 and T2). Despite the lower values (Table 1), both remained within the range considered normal for the studied species (Rezagholizadeh et al., 2015; Křížková et al., 2017; Gaitskell-Phillips et al., 2021). As can be seen in Table 1, the total motility remained practically constant for CG, T1 and T2, confirming changes only in the progressive motility and suggesting the presence of a residual number of SMNPs, probably in a nanometric range, which were not effectively attracted by the magnet and remained in suspension in the liquid medium causing a type of blockage to the free straight-line movement of the cells.

Nevertheless, considering the global set of evaluated parameters, the results obtained suggest the maintenance of fertilizing capacity of the equine spermatozoa (Love, 2011; Singh et al., 2021), confirming the biocompatibility of the SMNPs produced from secondary sources, as well as showing that the non-toxic silica layer plays an important role in this regard.

Fig. 8 depicts the in vitro test, in which a clear attraction between spermatozoa cells and SMNP-1 can be observed. It is intriguing that while some cells are completely immobilized due to a strong interaction between their head and the agglomerates of SMNPs (pink arrow), other cells show a free straight-lined journey across the medium (orange arrow) (Fig. 8a and c). The interaction between SMNPs and the studied cells can be evidenced in Fig. 8b, in which two agglomerates of approximately 5 μm each immobilize the same spermatozoon. The free movement of the cells, as well as their immobilization on SMNPs surface, can be seen in more details in Video 1 (https://drive.google.com/file/d/1IBMdrkFsHDpEO3s7zdbtUoBV1P_CvIQg/view?usp=sharing). The main result was a decrease on the number of free cells for both treatment groups in comparison to the control group ($P < 0.01$), which confirms the attraction of cells by the SMNPs surface (Table 2).

The nanoparticles based on iron oxide, as well as those containing silica, are recognized by their low toxicity and for this reason they are widely studied for multiple uses in the biomedical field (Berry and Curtis, 2003; Azam et al., 2012; Yaqoob et al., 2020). On the other hand, it is well known that some aspects related to the interaction between these materials and the organisms can result in some kind of cytotoxicity, impacting directly in the physical, chemical and biological properties of the cells, which in turn is dependent on the size and dosage of the nanoparticles, as well as on the idiosyncrasy of a given animal species (Exbrayat et al., 2015). Based on our results, only the features that encompass low toxicity were confirmed for the studied SMNPs, since all the seminal parameters linked to the fertility were not affected. Additionally, the progressive motility, which showed a decrease after the treatment with SMNPs, remained within the standards of quality required for the studied species.

The selective attraction observed between some spermatozoa and the SMNPs, which resulted in a dropdown of the spermatozoa concentration in the sample and subsequent reduction of the total cell count, as well as the clear absence of attraction to the other set of cells within the same sample, suggest similarities to what was reported by Domínguez et al. (2018), who monitored the attraction of only male gametes for magnetic nanoparticles during 5 min of treatment, and recommended the use of this type of materials for spermatic sexing of the equine species.

Certainly, further studies are necessary in order to enhance the comprehension of the interaction between SMNPs and the animal cells. The possible toxicity of the waste-based nanoparticles is one of the most important aspects that deserve deeper studies. Moreover, successive tests involving different individuals may reveal an existence of singular variations in the results. Notwithstanding, in vivo studies using semen treated by SMNPs, followed by insemination of females and a meticulous monitoring of the offspring's birth are fundamental for the development of technologies based on magnetic nanoparticles. Also, tests involving different species can help to elucidate the details of the interaction of SMNPs and cells, considering their distinct seminal characteristics.

In general, the results showed that the presence of a silica coating on the magnetite nanoparticles was essential for trapping the eventual heavy metals that could be dragged from the iron(II) input obtained from secondary sources into the final product.

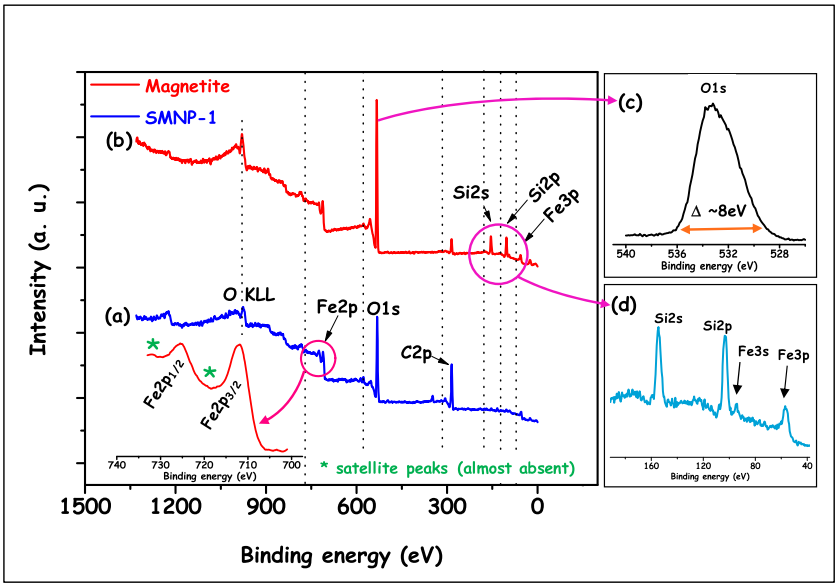

Fig. 7. XPS analysis of the (a) control magnetite showing Fe and O peaks, (b) SMNP-1 sample with silicon from silica shell, (c) a broad peak of oxygen, and (d) a detail of the Fe3s and Fe3p signals outermost electronic layers. (For interpretation of the references to colour in this figure legend, the reader is referred to the Web version of this article.)

Table 1
Results obtained from the CASA analysis system (average ± SD) for the studied parameters.

Parameter	CG	T1	T2
Vigor	3.4 ± 0.1	3.2 ± 0.2	3.4 ± 0.3
TM	73.3 ± 1.8	74.5 ± 7.1	74.2 ± 7.5
PM	61.7 ± 6.7[a]	48.9 ± 6.1[b]	48.3 ± 11.1[b]
VSL	66.8 ± 3.7	57.8 ± 3.8	58.4 ± 10.5
VCL	228.1 ± 5.0	214.7 ± 10.3	218.2 ± 18.3
VAP	100.9 ± 1.6	95.1 ± 5.1	96.4 ± 10.5

The superscripts [a] and [b] in the average values represent discrepancies in relation to the variance test ANOVA ($P < 0.05$). Vigor (Vig-1 to 5), Total Motility (TM, %), Progressive Motility (PM, %), curvilinear velocity (VCL, μms^{-1}), linear velocity (VSL, μms^{-1}), and average path velocity (VAP, μms^{-1}).

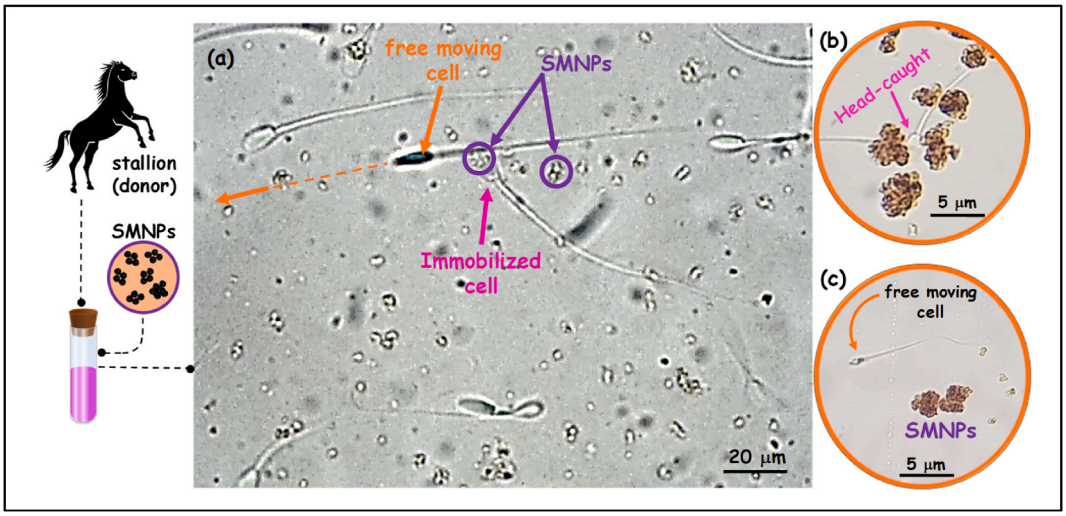

Fig. 8. Tests in vitro highlighting the interaction between cells and SMNPs.

Table 2
Results obtained in sperm concentration compared to the control group.

Parameter	CG	T1	T2
[ ] x10^6 mL^{-1}	51 ± 1.2^a	32.5 ± 4.3^b	25.9 ± 4.2^b
%	100.0	63.7	50.8

Average values marked ^{a} and ^{b} diverge from the result of the control group according to the Variance Test ANOVA ($P < 0.01$). In all experiments, the amount of cells was ~500 × 10^6. CG = Control group, T1 = Treatment group number 1, T2 = Treatment group number 2, [ ] = concentration (x10^6 mL^{-1}) and % = percentage of cells present in the medium considering the CG as 100%.

4. Conclusion

The green synthesis of silica-coated magnetite nanoparticles was not significantly interfered by the waste-based iron precursor source used for. All characterization techniques confirmed the successful production of crystalline-coated-ferromagnetic nanoparticles. The agglomeration of the nanoparticles was observed by SEM and DLS analyses, and their size was strongly influenced by the ultrasound treatment. Hazardous contaminants (heavy metals) from waste-based precursor were not detected and the SMNPs could be evaluated in vitro. The tests showed that the spermatozoa can be immobilized by their head, requiring a fine tune of their zeta potential for specific biomedical applications. In addition, in vitro tests revealed the high capacity of the SMNPs to concentrate the spermatozoon cells in the system. The CASA analysis performed in this study confirmed the biocompatibility of the synthesized SMNPs and reinforced the possibility of application of the nanomaterials for biomedical purposes.

Author statement

Conceptualization: Alesandro Bail and Mauro Flores Polenz. Data curation: Alesandro Bail and Mauro Flores Polenz. Formal analysis: Alesandro Bail and Mauro Flores Polenz. Funding acquisition: Alesandro Bail. Investigation: Alesandro Bail, Mauro Flores Polenz, Eduardo Malschitzky and Luis Guilherme Giannina Sante. Methodology: Mauro Flores Polenz, Alesandro Bail and Luis Guilherme Giannina Sante. Project administration: Alesandro Bail. Resources: Alesandro Bail. Software: Mauro Flores Polenz. Supervision: Alesandro Bail and Eduardo Malschitzky. Validation: Alesandro Bail, Mauro Flores Polenz and Eduardo Malschitzky. Writing - original draft: Alesandro Bail, Mauro Flores Polenz and Luis Guilherme Giannina Sante. Writing - review and editing: Alesandro Bail.

Declaration of competing interest

The authors declare the following financial interests/personal relationships which may be considered as potential competing interests:

Alesandro Bail reports financial support was provided by National Council for Scientific and Technological Development. Alesandro Bail reports financial support was provided by Coordination of Higher Education Personnel Improvement.

Acknowledgments

The authors acknowledge the financial support obtained from National Council for Scientific and Technological Development (CNPq) (grant number 436108/2018–6) for financial support and scholarship, Coordenação de Aperfeiçoamento de Pessoal de Nível Superior (CAPES) and Araucária Foundation. They are also thankful for the technical support of the LabMult – the Multi-User Laboratory of the UTFPR (Universidade Tecnológica Federal do Paraná).

Appendix A. Supplementary data

Supplementary data to this article can be found online at https://doi.org/10.1016/j.scp.2022.100678.

References

Ahmad, H., Hariyanto, B., Sulthonol, M., Klyusubun, W., Darminto, D.D., Pratapa, S., 2019. Structure and magnetic properties of silica-coated magnetite-nanoparticle composites. Mater. Res. Express 6, 086117. https://doi.org/10.1088/2053-1591/ab29af.

Azam, A., Ahmed, A.S., Oves, M., Khan, M.S., Habib, S.S., Memic, A., 2012. Antimicrobial activity of metal oxide nanoparticles against Gram-positive and Gram-negative bacteria: a comparative study. Int. J. Nanomed. 7, 6003–6009. https://doi.org/10.2147/IJN.S35347.

Baltrusaitis, J., Usher, C.R., Grassian, V.H., 2007. Reactions of sulfur dioxide on calcium carbonate single crystal and particle surfaces at the adsorbed water carbonate interface. Phys. Chem. Chem. Phys. 9, 3011–3024. https://doi.org/10.1039/b617697f.

Berry, C.C., Curtis, A.S.G., 2003. Functionalisation of magnetic nanoparticles for applications in biomedicine. J. Phys. D: Appl. 36, 198–206. https://doi.org/10.1088/0022-3727/36/13/203.

Bhat, T.S., Vanalakar, S.A., Devan, R.S., Mali, S.S., Pawar, S.A., Ma, Y.R., Hong, C.K., Kim, J.H., Patil, P.S., 2016. Compact nanoarchitectures of lead selenide via successive ionic layer adsorption and reaction towards optoelectronic devices. J. Mater. Sci. Mater. Electron. 27, 4996–5005. https://doi.org/10.1007/s10854-016-4386-8.

Cardoso, V.F., Francesko, A., Ribeiro, C., Bañobre-López, M., Martins, P., Lanceros-Mendez, S., 2017. Advances in magnetic nanoparticles for biomedical applications. Adv. Healthcare Mater. 7, 1700845–1700879. https://doi.org/10.1002/adhm.201700845.

Chang, Q.-Q., Cui, Y.-W., Zhang, H.-H., Chang, F., Zhu, B.-H., Yu, S.-Y., 2019. C-doped ZnO decorated with Au nanoparticles constructed from the metal–organic framework ZIF-8 for photodegradation of organic dyes. RSC Adv. 9, 12689–12695. https://doi.org/10.1039/c8ra09985e.

Cunha, T.N.D., Trindade, D.G., Canesin, M.M., Effting, L., Moura, A.A., Moisés, M.P., Junior, I.L.C., Bail, A., 2021. Reuse of waste pickling acid for the production of hydrochloric acid solution, iron(II) chloride and magnetic iron oxide: an eco-friendly process. Waste Biomass. Valor. 12, 1517–1528. https://doi.org/10.1007/s12649-020-01079-1.

Domínguez, E., Moreno-Irusta, A., Castex, H.R., Bragulat, A.F., Ugaz, C., Clemente, H., Giojalas, L., Losinno, L., 2018. Sperm sexing mediated by magnetic nanoparticles in donkeys, a preliminary in vitro study. J. Equine Vet. Sci. 65, 123–127. https://doi.org/10.1016/j.jevs.2018.04.005.

Dou, Z., Toth, J.D., Westendorf, M.L., 2018. Food waste for livestock feeding: feasibility, safety, and sustainability implications. Glob. Food Sec 17, 154–161. https://doi.org/10.1016/j.gfs.2017.12.003.

Eastmond, E.A., MacGregor, J.T., Slesinski, R.S., 2008. Trivalent chromium: assessing the genotoxic risk of an essential trace element and widely used human and animal nutritional supplement. Crit. Rev. Toxicol. 38, 173–190. https://doi.org/10.1080/10408440701845401.

Exbrayat, J.M., Moudilou, E.N., Lapied, E., 2015. Harmful effects of nanoparticles on animals. J. Nanotechnol. 2015, 1–10. https://doi.org/10.1155/2015/861092.

Foroozandeh, P., Aziz, A.A., 2018. Insight into cellular uptake and intracellular trafficking of nanoparticles. Nanoscale Res. Lett. 13, 339–350. https://doi.org/10.1186/s11671-018-2728-6.

Friege, H., 2017. Sustainable chemistry – a concept with important links to waste management. Sustain. Chem. Pharm. 6, 57–60. https://doi.org/10.1016/j.scp.2017.08.001.

Fu, Z., Hu, J., Hu, W., Yang, S., Luo, Y., 2018. Quantitative analysis of Ni^{2+}/Ni^{3+} in $Li[Ni_xMn_yCo_z]O_2$ cathode materials: non-linear least-squares fitting of XPS spectra. Appl. Surf. Sci. 441, 1048–1056. https://doi.org/10.1016/j.apsusc.2018.02.114.

Gaitskell-Phillips, G., Martín-Cano, F.E., Ortiz-Rodríguez, J.M., Silva-Rodríguez, A., Silva-Álvarez, E., Rojo-Domínguez, P., Tapia, J.A., Gil, M.C., Ortega-Ferrusola, C., Peña, F.J., 2021. Proteins involved in mitochondrial metabolic functions and fertilization predominate in stallions with better motility. J. Proteonomics 247, 104335–104346. https://doi.org/10.1016/j.jprot.2021.104335.

Guo, T., Lin, M., Huang, J., Zhou, C., Tian, W., Yu, H., Jiang, X., Ye, J., Shi, Y., Xiao, Y., Bian, X., Feng, X., 2018. The recent advances of magnetic nanoparticles in medicine. J. Nanomater. 2018, 1–8. https://doi.org/10.1155/2018/7805147.

Hu, G.W., Zeng, L.C., Du, H., Wang, Q., Fan, Z.T., Liu, X.W., 2021. Combined effects of solute drag and Zener pinning on grain growth of a NiCoCr medium-entropy alloy. Intermetallics 136, 107271–107279. https://doi.org/10.1016/j.intermet.2021.1072.

Jacomaci, N., Junior, E.S., Oliveria, F.M.B., Longo, E., Zaghete, M.A., 2019. Dielectric behavior of α-Ag_2WO_4 and its huge dielectric loss tangent. Mat. Res. 22, e20190058 https://doi.org/10.1590/1980-5373-MR-2019-0058.

Jin, L., Chai, L., Ren, L., Jiang, Y., Yang, W., Wang, S., Liao, Q., Wang, H., Zhang, L., 2019. Enhanced adsorption-coupled reduction of hexavalent chromium by 2D poly(m-phenylenediamine)-functionalized reduction graphene oxide. Environ. Sci. Pollut. Res. 29, 31099–31110. https://doi.org/10.1007/s11356-019-06175-x.

Joseph, B., James, J., Kalarikkal, N., Thomas, S., 2021. Recycling of medical plastics. Adv. Ind. Eng. Polymer Res 4, 199–208. https://doi.org/10.1016/j.aiepr.2021.06.003.

Kelgenbaeva, Z., Omurzak, E., Takebe, S., Abdullaeva, Z., Sulaimankulova, S., Iwamoto, C., Mashimo, T., 2013. Magnetite nanoparticles synthesized using pulsed plasma in liquid. Jpn. J. Appl. Phys. 52, 11NJ02. https://doi.org/10.7567/jjap.52.11nj02.

Kemp, S.J., Ferguson, R.M., Khandhar, A.P., Krishnan, K.M., 2016. Monodisperse magnetite nanoparticles with nearly ideal saturation magnetization. RSC Adv. 6, 77452–77464. https://doi.org/10.1039/c6ra12072e.

Křížková, J., Čoudková, V., Maršálek, M., 2017. Computer assisted sperm analysis (CASA) of head morphometry and kinematic parameters in Warmblood stallions spermatozoa. J. Equine Vet. Sci. 57, 8–17. https://doi.org/10.1016/j.jevs.2017.05.012.

Kumar, B., Smita, K., Cumbal, L., Debut, A., Galeas, S., Guerrero, V.H., 2016. Phytosynthesis and photocatalytic activity of magnetite (Fe_3O_4) nanoparticles using the Andean blackberry leaf. https://doi.org/10.1016/j.matchemphys.2016.05.045, 179,310-315.

Kumari, P., Alam, M., Siddiqi, W.A., 2019. Usage of nanoparticles as adsorbents for waste water treatment: an emerging trend. Sustain. Mater. Technol., e00128 https://doi.org/10.1016/j.susmat.2019.e00128.

Langford, J.I., Wilson, A.J.C., 1978. Scherrer after sixty years: a survey and some new results in the determination of crystallite size. J. Appl. Crystallogr. 11, 102–113. https://doi.org/10.1107/s0021889878012844.

Larentis, G.R., Camozzato, G.C., Bastos, H.B.A., Gregory, R.M., Mattos, R.C., 2018. Equine sperm selection by synthetic membrane filter. J. Equine Vet. Sci. 63, 69–73. https://doi.org/10.1016/j.jevs.2018.01.013.

Li, Q., Kartikowati, C.W., Horie, S., Ogi, T., Iwaki, T., Okuyama, K., 2017. Correlation between particle size/domain structure and magnetic properties of highly crystalline Fe_3O_4 nanoparticles. Sci. Rep. 7, 9894–9900. https://doi.org/10.1038/s41598-017-09897-5.

Love, C.C., 2011. Relationship between sperm motility, morphology and the fertility of stallions. Theriogenology 76, 547–557. https://doi.org/10.1016/j.theriogenology.2011.03.007.

Mandel, K., Straßer, M., Granath, T., Dembski, S., Sextl, G., 2015. Surfactant free superparamagnetic iron oxide nanoparticles for stable ferrofluids in physiological solutions. Chem. Commun. (J. Chem. Soc. Sect. D) 51, 2863–2866. https://doi.org/10.1039/c4cc09277e.

Matlin, S.A., Mehta, G., Hopf, H., Krief, A., Keßler, L., Kümmerer, K., 2020. Material circularity and the role of the chemical sciences as a key enabler of a sustainable post-trash age. Sustain. Chem. Pharm. 17, 100312. https://doi.org/10.1016/j.scp.2020.100312.

Monteiro, A., Santos, S., Gonçalves, P., 2021. Precision agriculture for crop and livestock Farming - brief review. Animals 11, 2345–2362. https://doi.org/10.3390/ani11082345.

Novoselova, L.Y., 2021. Nanoscale magnetite: new synthesis approach, structure and properties, Appl. Surf. Sci. 539, 148275. https://doi.org/10.1016/j.apsusc.2020.148275.

Özdemir, T., Öztin, C., Kıncal, N.S., 2006. Treatment of waste pickling liquors: process synthesis and economic analysis. Chem. Eng. Commun. 193, 548–563. https://doi.org/10.1080/00986440500192238.

Pasandideh, E.K., Kakavandi, B., Nasseri, S., Mahvi, A.H., Nabizadeh, R., Esrafili, A., Kalantary, R.R., 2016. Silica-coated magnetite nanoparticles coreshell spheres (Fe_3O_4@SiO_2) for natural organic matter removal. J. Environ. Health Sci. Eng. 14, 21–33. https://doi.org/10.1186/s40201-016-0262-y.

Rahmawati, R., Permana, M.G., Harison, B., Nugraha, Yuliarto, B., 2017. Optimization of frequency and stirring rate for synthesis of magnetite (Fe_3O_4) nanoparticles by using coprecipitation - ultrasonic irradiation methods. Procedia Eng. 170, 55–59. https://doi.org/10.1016/j.proeng.2017.03.010.

Rezagholizadeh, A., Gharagozlou, F., Niasari-Naslaji, A., Akbarinejad, V., Ziapour, S., 2015. Evaluation of sperm characteristics in Caspian stallions using computer-assisted sperm analysis. J. Equine Vet. Sci. 35, 505–509. https://doi.org/10.1016/j.jevs.2015.02.003.

Rodriguez, A.F.R., Costa, T.P., Bini, R.A., Faria, F.S.E.D.V., Azevedo, R.B., Jafelicci, M., Coaquira, J.A.H., Martínez, M.A.R., Mantilla, J.C., Marques, R.F.C., Morais, P.C., 2017. Surface functionalization of magnetite nanoparticle: a new approach using condensation of alkoxysilanes. Phys. B Condens. Matter 521, 141–147. https://doi.org/10.1016/j.physb.2017.06.043.

Safari, J., Gandomi-Ravandia, S., Haghighia, Z., 2016. Supported polymer magnets with high catalytic performance in the green reduction of nitroaromatic compounds. RSC Adv. 6, 31514–31525. https://doi.org/10.1039/C5RA26613K.

Samrot, A.V., Sahithya, C.S., Selvarani, A.J., Purayil, S.K., Ponnaiah, P., 2021. A review on synthesis, characterization and potential biological applications of superparamagnetic iron oxide nanoparticles. Curr. Res. Green Sustain. Chem. 4, 100042. https://doi.org/10.1016/j.crgsc.2020.100042.

Shabana, M.S., Taju, G., Majeed, S.A., Ahmed, A.N., Karthika, M., Ramasubramanian, V., Hameed, A.S.S., 2021. Preparation and evaluation of mesoporous silica nanoparticles loaded quercetin against bacterial infections in Oreochromis niloticus. Aquaculture Reports 21, 100808–100819. https://doi.org/10.1016/j.aqrep.2021.100808.

Shahid, M.K., Kim, Y., Choi, Y.-G., 2019. Magnetite synthesis using iron oxide waste and its application for phosphate adsorption with column and batch reactors. Chem. Eng. Res. Des. 148, 169–179. https://doi.org/10.1016/j.cherd.2019.06.001.

Sharma, R.K., Yadav, M., Monga, Y., Gaur, R., Adholeya, A., Zboril, R., Varma, R.S., Gawande, M.B., 2016. Silica-based magnetic manganese nanocatalyst - applications in the oxidation of organic halides and alcohols. ACS Sustain. Chem. Eng. 4, 1123–1130. https://doi.org/10.1021/acssuschemeng.5b01183.

Silva, V.A.J., Andrade, P.L., Silva, M.P.C., Bustamante, D.A., De Los Santos Valladares, L., Albino Aguiar, J., 2013. Synthesis and characterization of Fe_3O_4 nanoparticles coated with fucan polysaccharides. J. Magn. Magn Mater. 343, 138–143. https://doi.org/10.1016/j.jmmm.2013.04.062.

Singh, A.K., Kumar, A., Bisla, A., 2021. Computer-assisted sperm analysis (CASA) in veterinary science: a review. Indian J. Anim. Sci. 91, 419–429. https://doi.org/10.1016/j.theriogenology.2013.09.004.

Sonmez, M., Georgescu, M., Alexandrescu, L., Gurau, D., Ficai, A., Ficai, D., Andronescu, E., 2015. Synthesis and applications of Fe_3O_4/SiO_2 core-shell materials. Curr. Pharmaceut. Des. 21, 5324–5325. https://doi.org/10.2174/1381612821666150917094031.

Sun, J., Zhou, S., Hou, P., Yang, Y., Weng, J., Li, X., Li, M., 2006. Synthesis and characterization of biocompatible Fe_3O_4 nanoparticles. J. Biomed. Mater. Res. 80, 333–341. https://doi.org/10.1002/jbm.a.30909.

Tanabe, K., Sumiyoshi, T., Shibata, K., Kiyoura, T., Kitagawa, J., 1974. A new hypothesis regarding the surface acidity of binary metal oxides. Bull. Chem. Soc. Jpn. 47, 1064–1066. https://doi.org/10.1246/bcsj.47.1064.

Tang, J., Pei, Y., Hu, Q., Pei, D., Xu, J., 2016. The recycling of ferric salt in steel pickling liquors: preparation of nano-sized iron oxide. Procedia Environ. Sci. 31, 778–784. https://doi.org/10.1016/j.proenv.2016.02.071.

Tian, Y., Yu, B., Li, X., Li, K., 2011. Facile solvothermal synthesis of monodisperse Fe_3O_4 nanocrystals with precise size control of one nanometre as potential MRI contrast agents. J. Mater. Chem. 21, 2476. https://doi.org/10.1039/c0jm02913k.

Thornton, P.K., 2010. Livestock production: recent trends, future prospects. Philos. Trans. R Soc B 365, 2853–2867. https://doi.org/10.1098/2Frstb.2010.0134.

Tortajada, C., van Rensburg, P., 2019. Drink more recycled wastewater. Nature 577, 26–28. https://doi.org/10.1038/d41586-019-03913-6.

Tortajada, C., 2020. Contributions of recycled wastewater to clean water and sanitation sustainable development goals. NPJ Clean Water 22, 1–6. https://doi.org/10.1038/s41545-020-0069-3.

Tran, H.-V., Ngo, N.M., Medhi, R., Srinoi, P., Liu, T., Rittikulsittichai, S., Lee, T.R., 2022. Multifunctional iron oxide magnetic nanoparticles for biomedical applications: a Review. Materials 15, 503. https://doi.org/10.3390/ma15020503.

Tsai, C.-H., Shen, Y.-H., Tsai, W.-T., 2021. Sustainable material management of industrial hazardous waste in Taiwan: case studies in circular economy. Sustainability 13, 9410–9420. https://doi.org/10.3390/su13169410.

UN - The United Nations, 2022. The Sustainable Development Agenda. https://www.un.org/sustainabledevelopment/development- agenda/. (Accessed 25 February 2022).

Višak, T., Garner, R., 2016. The Ethics of Killing Animals, first ed. Oxford University Press, New York. https://doi.org/10.1093/acprof:oso/9780199396078.001.0001.

Wang, J.-C., Rena, J., Yao, H.-C., Zhang, L., Wang, J.-S., Zang, S.-Q., Han, L.-F., Li, Z.-J., 2016. Synergistic photocatalysis of Cr(VI) reduction and 4-chlorophenol degradation over hydroxylated α-Fe_2O_3 under visible light irradiation. J. Hazard Mater. 311, 11–19. https://doi.org/10.1016/j.jhazmat.2016.02.055.

Wang, X., Lv, F., 2018. Synthesis of Fe_3O_4 magnetic powder from spent pickling liquors. Trans. Tianjin Univ. 24, 45–50. https://doi.org/10.1007/s12209-017-0095-5.

Yaqoob, A.A., Ahmad, H., Parveen, T., Ahmad, A., Oves, M., Ismail, I.M.I., Qari, H.A., Umar, K., Mohamad, I.M.N., 2020. Recent advances in metal decorated nanomaterials and their various biological applications: a review. Front. Chem. 8, 341–363. https://doi.org/10.3389/fchem.2020.00341.

Zelepukin, I.V., Shipunova, V.O., Mirkasymov, A.B., Nikitin, P.I., Nikitin, M.P., Deyev, S.M., 2017. Synthesis and characterization of hybrid core-shell Fe_3O_4/SiO_2 nanoparticles for biomedical applications. Acta Naturae 9, 58–65.

Zhang, W., Lu, B., Tang, H., Zhao, J., Cai, Q., 2015. Reclamation of acid pickling waste: a facile route for preparation of single-phase Fe_3O_4 nanoparticle. J. Magn. Magn Mater. 381, 401–404. https://doi.org/10.1016/j.jmmm.2015.01.037.

Zueva, S.B., Ferella, F., Innocenzi, V., De Michelis, I., Corradini, V., Ippolito, N.M., Vegliò, F., 2021. Recovery of zinc from treatment of spent acid solutions from the pickling stage of galvanizing plants. Sustainability 13, 407–414. https://doi.org/10.3390/su13010407.